J Mater Sci: Mater Med (2010) 21:2463–2477
DOI 10.1007/s10856-010-4095-4

Methodologies for assessing local surface texture features that are relevant to cell attachment

Alistair Forbes · Paul Tomlins · Elzbieta Gurdak · Matthew Illsely · Stuart James · Elizabeth James

Received: 20 August 2009 / Accepted: 5 May 2010 / Published online: 28 May 2010

Abstract In this paper, we describe techniques for extracting features from surface topography data, gathered by a 3D-microscopy system, on a length scale that is relevant for cell attachment. The feature parameters considered include standard surface roughness parameters applied to the complete surface as well as new feature parameters designed to quantify local variations in surface topography potentially influencing cell behaviour. Methodologies have been developed both to determine the degree of homogeneity or isotropy of a surface and to compare the topographies of different samples. The approaches followed include wavelet decomposition and linear and nonlinear filtering techniques. The analysis has been used to investigate the correlation between osteoblast cell attachment and structural features of titanium-coated surfaces representative of orthopaedic implants. The results confirm that there is a discernible correlation between cell orientation and the underlying surface lay.

1 Introduction

It has long been established that the behaviour of cells on a surface is influenced by its chemistry, topography and energy [1–4]. These attributes of the surface are usually difficult to segregate because of their interdependence, however it has been convincingly demonstrated that cells are more sensitive to topographical cues than to the chemistry [5, 6] and therefore energy [7] of the surface. The cell response behaviour has been exploited to some extent in the design and finish of orthopaedic implants. However, the relationship between cell behaviour and surface texture, despite much research activity, is still not fully understood. Studies of cell surface interactions focus on either using randomly textured surfaces [8, 9] or surfaces that have a well-defined periodic structure, e.g., grooves [10] or pillars [11]. Early studies in this field focused on the creation of micrometre scale surface features but more recently there has been a move to study the effects that nanoscale features have on cell behaviour [12]. Variola et al. [13] showed that the sponge-like nanotexture created by etching titanium alloy samples enhances the proliferation rate of osteoblastic cells and retards that of fibroblastic cells compared to smooth control samples. Dalby et al. [14] have shown that human mesenchymal stem cells present in bone marrow exhibit more osteoblastic morphology and improved differentiation on surfaces that had randomly distributed nanoscale features, such as wells, compared with hexagonal or square arrays of the same features. Ranucci and Moghe showed that roughening the surface of poly (glycolic-co-lactic) acid at the micrometre level enhanced the attachment and adhesive strength of osteoblast-like cells [15]. The extensive work of Curtis et al. [10, 16–18] has shown that topographical guidance in the form of micro-grooves determines the shape and movement of the majority of cell types. However, it is still unclear whether cells are more sensitive to the depth of the groove or the spacing between them [17].

A common challenge for the characterization of surface texture at both the micro- and nano-level is how to define quantitative measures that describe the overall roughness,

A. Forbes (✉) · P. Tomlins · E. Gurdak
National Physical Laboratory, Hampton Road, Teddington TW11 OLW, UK
e-mail: alistair.forbes@npl.co.uk

P. Tomlins
e-mail: paul.tomlins@npl.co.uk

M. Illsely · S. James · E. James
University of Brighton, Brighton, UK

account for differences in structural homogeneity and highlight the importance of specific features, e.g., peak heights, density of peaks, etc. The majority of papers use global measures of topography that are based on the analysis of 2D profiles extracted at right angles to the lay of a surface that has periodic features, or at a random orientation for an aperiodic surface. The principle parameter used to describe these 2D surface profiles is the arithmetic mean of the absolute deviations of the ordinate values of a profile, *Ra* [19–21]. It is important to recognize that this parameter, by its definition, is only sensitive to average variation in the amplitude of the surface heights and does not reflect variation in local behaviour. Consequently, surfaces with quite different textures can have similar values of *Ra*.

Quantification of surfaces using 2D profiles has been, and continues to be, extensively used in engineering. More recently a complementary suite of parameters have been derived that describe 3D areal textures. The 3D areal parameters are divided into four categories: amplitude, spatial, hybrid and functional [22, 23]. The extension to a third dimension provides the potential for a more detailed description of the surface, for example, the orientation of features such as ridges or grooves. Recently, Sosale et al. [24] used the full range of areal parameters to quantify differences in the topography over two length scales (nanometre and micrometre) of two titanium alloy implants which elicit different bone responses. The surfaces were prepared by either grit-blasting (GB) or grit-blasting followed by acid-etching (GB + AE) and measured using white light interferometry and atomic force microscopy. The GB + AE surfaces triggered a better response than GB finished surfaces. The average difference over all the derived parameters was less than 20% but the root-mean-square slope and summit curvature differed by 63% and 75%, respectively, suggesting that these parameters are particularly sensitive measures for characterising surfaces in this application.

Despite the advances in 3D surface texture analysis made during the past 10 years, surface texture parameters are largely global measures that are not particularly useful in identifying causal relationships between cell behaviour and local features. In this paper, we describe techniques for quantifying local texture and the degree of homogeneity and isotropy over a surface. In Sect. 2, we describe the experimental approach for acquiring data for the analysis of surface topography and cell adhesion while in Sect. 3 we discuss techniques for analysing surface topography, focusing first on homogeneity and then isotropy. The techniques are illustrated using a number of surfaces. In Sect. 4, we discuss methods for correlating cell behaviour with surface topography. Our concluding remarks are given in Sect. 5.

2 Materials and methods

2.1 Titanium samples

Test surfaces in the form of discs, 12 mm in diameter and 1.5 mm in thickness were cut from nickel comparator specimens (Rubert & Co Ltd.). Comparator specimens are used for roughness comparison measurements and typically consist of eight differently textured zones produced by different machining techniques/finishes. Specimens 331 and 315 were used; these are produced by spark erosion and grinding respectively. Three discs were cut from each comparator specimen with *Ra* values of 0.4 μm, 3.2 μm and 12.5 μm for plate 331 and *Ra* values of 0.025 μm, 0.2 μm and 3.2 μm for plate 315. After cutting, the discs were magnetron sputter coated with 99.5% (grade 2) titanium to a depth of approximately 500 nm (Teer Coatings Ltd.).

2.2 Cell adhesion study

Prior to use, the titanium discs were initially cleaned in 100% ethanol, disinfected with 70% ethanol and washed three times in sterile Hanks medium (Invitrogen). Two discs were used for the cell attachment studies and were exposed to an osteoblast line. The osteoblast line is the terminally differentiated osteosarcoma osteoblast-like SaoS2 cell line, used at an in-house passage 5, and an estimated supplier passage number of 120 (ATCC HTB-85, isol. 1977).

The test discs were placed in individual wells in a 24 well plate (Nunc). Two discs in duplicate were seeded with SaoS2 cells at a seeding density of 4.5×10^4 cells per cm^2 which yields 50% confluence on the disc surface. One disc in each set of three was seeded at 1.73×10^4 cells per cm^2 which again yields 50% confluence, that is, 4.39×10^4 cells were added to each well of area 2.5 cm^2. The same protocol was used to seed the same cells at the same densities on to the surface of the plastic in a separate set of empty wells to act as controls. (These controls were used only to assess qualitatively the consistency of cell behaviour between sets for experiments). The discs were cultured for 20.75 hrs in an humidified incubator at 37°C, and 5% CO_2.

The discs and control surfaces were washed gently four times in phosphate buffered saline (0.1 M, pH 7). The cells on the discs and plastic were then fixed in an acetone/methanol mixture (50/50) for 10 min, to both fix the cells and permeablise the membranes. The cells were then washed and post-fixed in 10% neutral buffered formal saline for 30 min and then washed gently in phosphate buffered saline (0.1 M, pH 7) three times. The cells were then covered in a solution of propidium iodide (Invitrogen) stain in buffered saline and left for 10 min before being

viewed under laser scanning confocal fluorescence microscopy (a 488 line-argon laser with excitation peak 535 nm, emission peak 617 nm) to confirm the presence or absence of cells.

2.3 Three-dimensional surface imaging

Three dimensional surface images along with x-, y-, and z-co-ordinates were captured using an optical microscope (Alicona Infinite Focus Microscope, Alicona Imaging GmbH). Six images of the sample were captured at × 20 magnification on each sample before and after exposure to cells ('before') and ('after'). Each sample disc was mounted in a purpose built jig before being placed under the microscope. This ensured that the images captured 'before' and 'after' were of the same areas of the surfaces within a tolerance of approximately ± 1.5 μm. The image size was 513.9 μm × 411.1 μm with the resolution set at 640 pixels × 512 pixels, i.e., a resolution of 0.8092 μm in x- and y-co-ordinates. The resolution in the z-co-ordinate for slow speed scanning was 50 nm. Binary masks of the adhered cells on the substrates were manually created from 8-bit grey scale images using Image J software (version 1.4). Figure 1 shows the microscope image of a ground surface and its graphical representation while Fig. 2 shows the corresponding microscope image recorded at the pre-defined co-ordinates with adhered cells (left) from which a binary mask was created (right).

3 Surface topography analysis

The goal of the surface topography analysis is to extract functionally relevant features from measurements of the surface. The image data provides 3-dimensional co-ordinates (x_{ij}, y_{ij}, z_{ij}) where the x- and y-co-ordinates nominally lie on a 640 × 512 pixel grid, with a grid spacing of 0.8092 μm in the x- and y-directions. Clearly, the information provided by the values of a small number of surface texture parameters associated with a set of co-ordinates on a 640 × 512 grid represents only a small fraction of the information contained in the complete set of co-ordinates. However, the data reflects random behaviour that can be summarised by parameters associated with statistical distributions (mean, standard deviation, etc.). In selecting a set of features, a balance has to be made between succinctness and loss of relevant information. What is relevant depends on the intended functionality of the surface. In recent years there has been much research activity in defining a modest number of features that are likely to be useful in summarising surface topography, see, e.g., [25–27]. The features discussed below have been chosen on the basis of relevance to cell adhesion and are computed for four example surfaces, labelled A, B, C and D for future reference. Figure 3 gives images of the two ground surfaces, A and B, and Fig. 4 gives the images of two spark eroded surfaces, C and D.

3.1 Global surface roughness parameters

The least-squares best fit plane to each measured surface was calculated and the heights z_{ij} adjusted so that the best-fit plane to the adjusted data is $z = 0$. Figures 5 and 6 graph the central 256 × 256 set of measurements for surfaces A, B, C and D (shown in Figs. 3, 4) with the best-fit plane removed. At a small scale, surface D is visibly smoother than surfaces A, B and C.

The following standard surface roughness parameters were calculated for each adjusted set of heights:

$$Sa = \frac{1}{N_x N_y}\sum_{i=1}^{N_x}\sum_{j=1}^{N_y}|z_{ij}|, \quad Sq = \left(\frac{1}{N_x N_y}\sum_{i=1}^{N_x}\sum_{j=1}^{N_y} z_{ij}^2\right)^{1/2},$$

$$Ssk = \frac{1}{(Sq)^3}\frac{1}{N_x N_y}\sum_{i=1}^{N_x}\sum_{j=1}^{N_y} z_{ij}^3, \quad Sku = \frac{1}{(Sq)^4}\frac{1}{N_x N_y}\sum_{i=1}^{N_x}\sum_{j=1}^{N_y} z_{ij}^4.$$

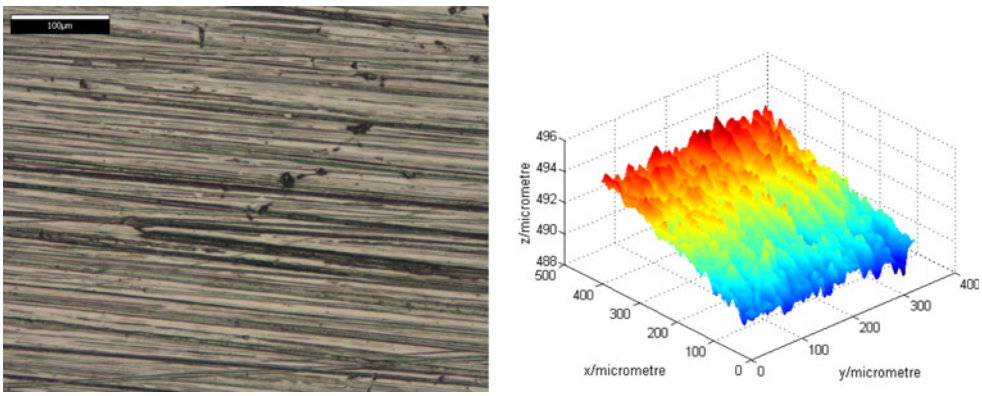

Fig. 1 Microscope image of a ground surface (*left*) and its graphical representation (*right*)

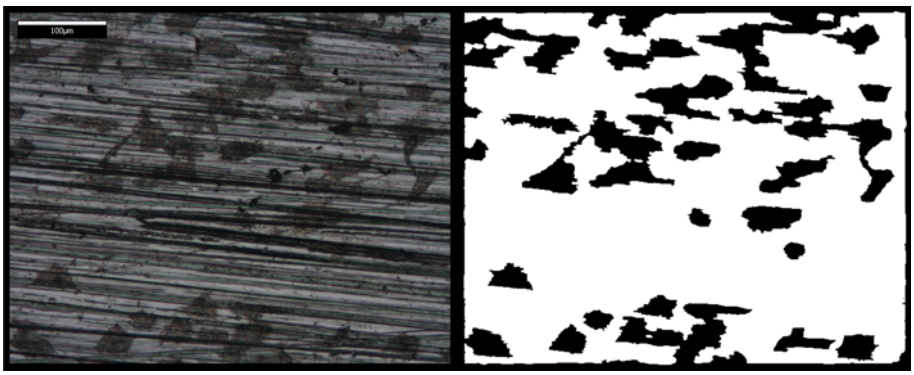

Fig. 2 Microscope image of the same surface in Fig. 1 with cells attached (*left*) and its corresponding binary cell mask (*right*)

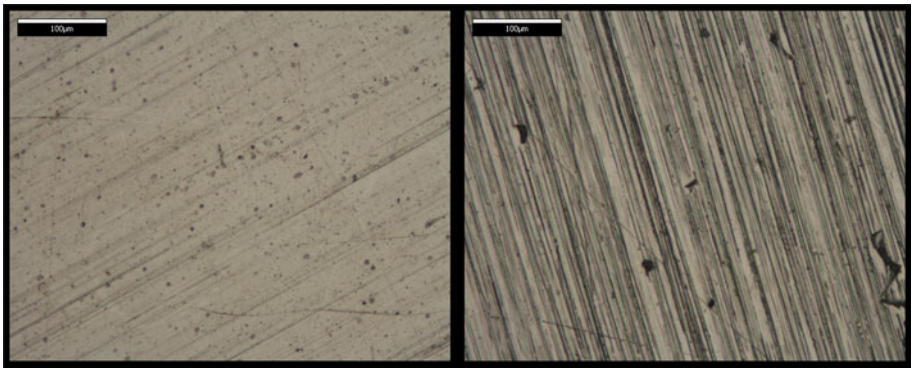

Fig. 3 Images of ground surfaces A, *left*, and B, *right*

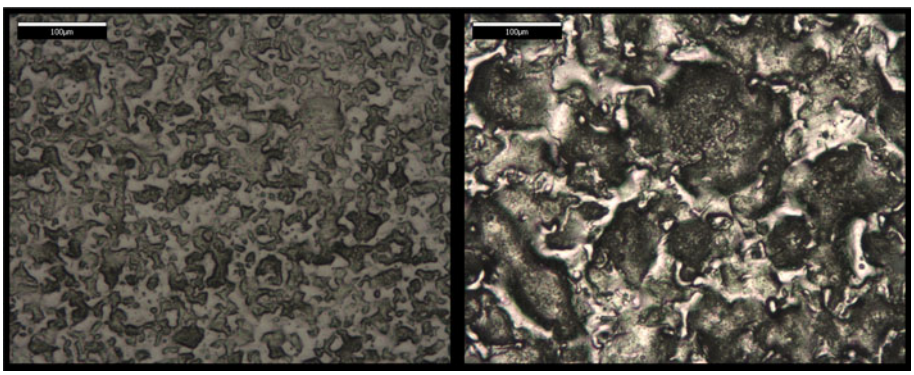

Fig. 4 Images of spark eroded surfaces C, *left*, and D, *right*

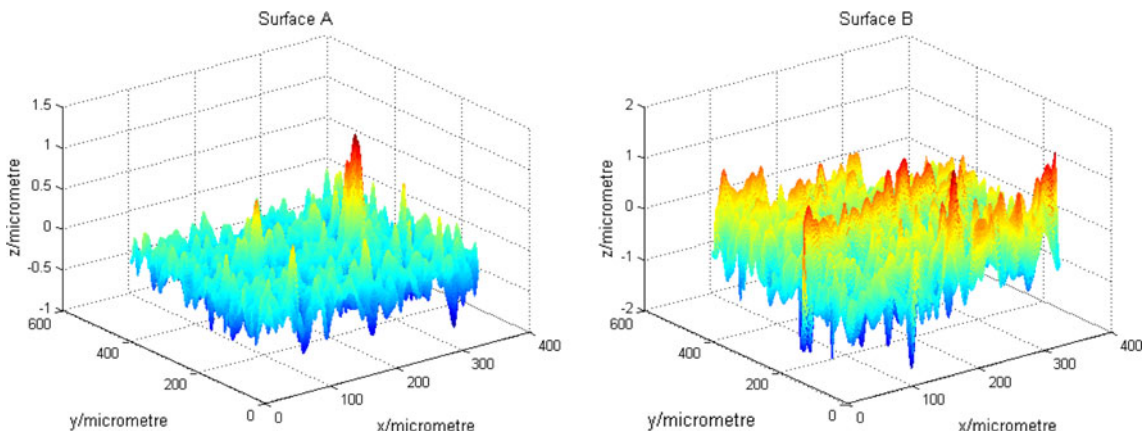

Fig. 5 Central 256 × 256 grid of measurements of ground surfaces A and B, with least-squares best-fit plane removed

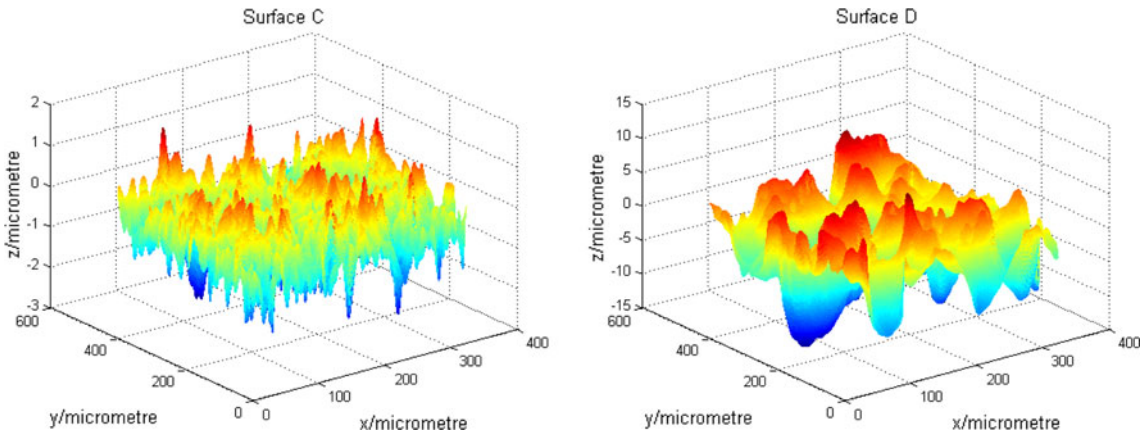

Fig. 6 As Fig. 5 but for spark eroded surfaces C and D. The z-axis scale for surface D is approximately 10 times that of surfaces A, B and C

Regarding the (adjusted) heights, z_{ij}, as samples from a probability distribution, Sq^2, *Ssk* and *Sku* are estimates of the distribution variance, skewness and kurtosis, respectively. A positive skewness parameter arises, for example, if the surface tends to have sharp peaks and broad valleys. Kurtosis is a measure of the 'peakedness' of a probability distribution. The definitions of the parameters *Sa*, *Sq*, *Ssk* and *Sku*, involve powers z^k, $k = 1, 2, 3, 4$, of the heights z and the larger the power, the more sensitive the corresponding parameter is to outlying data representing scratches, for example.

Table 1 gives the values of the parameters *Sa*, *Sq*, *Ssk* and *Sku* calculated for a 256 × 256 central grid of measurements for the surfaces A, B, C, and D; see Figs. 5 and 6. The Table also gives the calculated parameters for a random surface, labelled 'E', whose heights $z_{ij} \in N(0, 1)$ are drawn from a standard normal distribution. Surface D has a much larger *Sq* parameter value. The kurtosis parameter for surface A is large, due to the large isolated peak apparent in Fig. 5. The values of *Sq*, *Ssk* and *Sku* for the random Gaussian surface E are close to the expected values of 1, 0 and 3, respectively.

Table 1 Parameters *Sa*, *Sq*, *Ssk*, *Sku*, *Sds*, *Sl* and *Str* for real surfaces A, B, C, D, and a random surface E

Parameters	A	B	C	D	E
Sa (μm)	0.13	0.33	0.35	3.44	0.80
Sq (μm)	0.18	0.42	0.45	4.37	1.00
Ssk	1.13	0.09	−0.26	−0.68	0.00
Sku	10.29	3.44	3.66	3.20	3.01
$Sds \times 10^3$	3.95	3.36	3.95	0.75	166.66
Sl	0.82	0.18	0.83	0.56	0.92
Str	0.81	0.11	0.56	0.88	1.00

3.2 Spatial homogeneity

The global surface roughness parameters defined in 3.1 depend only on the values of the heights z_{ij} and not on how the heights are distributed on the surface. This section describes methods that give a measure of the degree of surface homogeneity as a function of location.

3.2.1 Wavelet analysis

A wavelet analysis of the surface co-ordinate data was performed in order to provide information at various length scales. The Haar wavelet was used as it can be directly related to the surface roughness parameter *Sq*. A Haar wavelet analysis can be described as follows. The *xy*-grid is partitioned into four equal squares and the mean values of the four sets of corresponding z-co-ordinates calculated. These four mean heights specify an approximation of the surface in terms of four step functions. This is the level 1 approximation. Each of the four squares is then partitioned into four sub-squares and the mean heights for each of the 16 sub-squares calculated. This provides a level 2 approximation to the surface. The process can be repeated until no further partitions are possible. At level k the mean heights can be stored into a parameter vector $\mathbf{a}_k$. The level k approximation $\hat{z}_{ij}(\mathbf{a}_k)$ to z_{ij} is given by the mean value for the sub-square containing the ijth grid point. The level 1 approximation represents the largest scale approximation, with the scales becoming smaller as the levels increase. The approximating surfaces can be calculated very efficiently using wavelet decomposition algorithms.

Figure 7 shows the level 2 and level 5 approximations to surface B (from Fig. 5) while Fig. 8 those for surface D (from Fig. 6).

Let S^2_k denote the variance of the kth level approximation $\hat{z}_{ij}(\mathbf{a}_k)$ and Sq^2 the variance of the complete surface, as before. The ratio

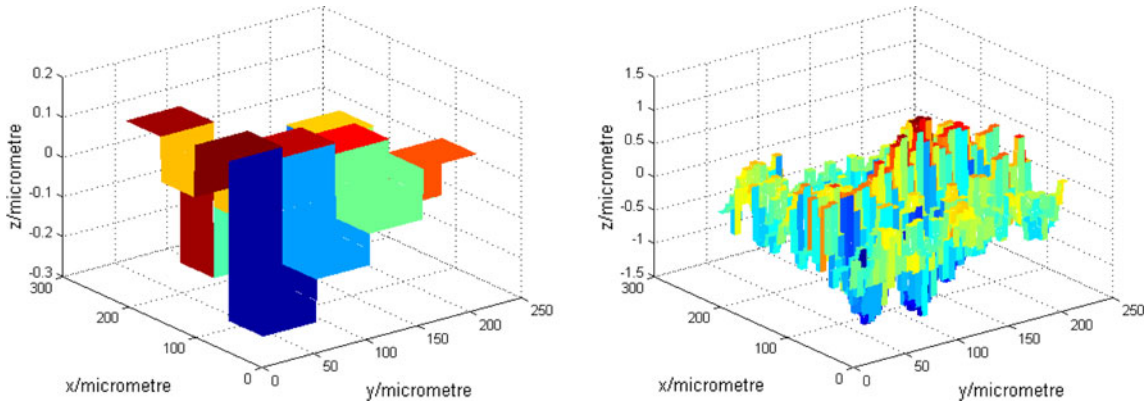

Fig. 7 Level 2 and 5 Haar wavelet approximations to surface B (shown in Fig. 5)

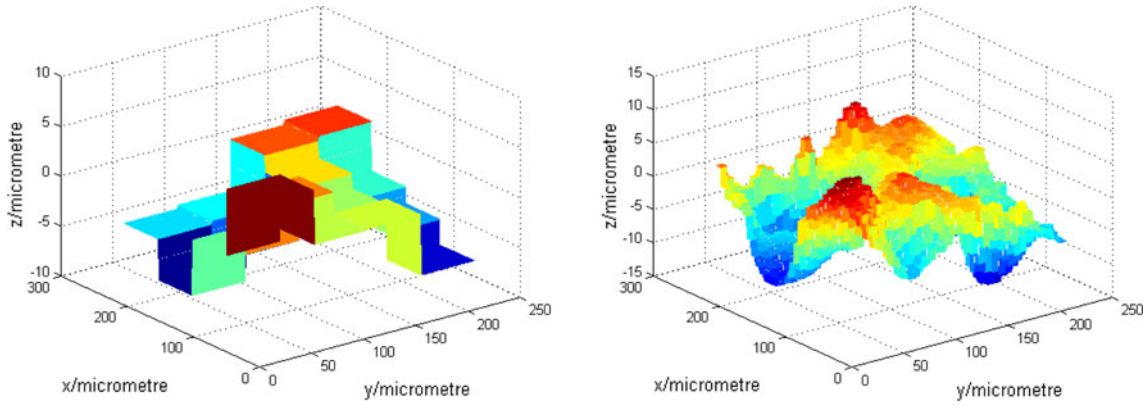

Fig. 8 As Fig. 7 but for surface D (shown in Fig. 6)

$$R_k = S_k^2/Sq^2, \tag{1}$$

is a measure of how much of the variation of the entire surface is explained by the kth level approximation. These ratios, as a function of level k, give a profile of how the surface can be resolved at different scales, i.e., provide a measure of the balance between coarse and fine features. Similarly, the difference $Sq_k^2 = Sq^2 - S_k^2$ is a measure of the variance once the level k approximation is removed.

The wavelet decomposition provides a partition of the variation of the surface according to the various levels and hence length scales. Figure 9 graphs the partition of variances from levels 1–8, coarse to fine, for the four surfaces A, B, C and D (Figs. 5, 6) and the Gaussian random surface E. Surfaces A, B and C have a similar partition profile with most of the variation of the surface explained at intermediate levels of scale. For surface D, the variance at levels 1 and 2 are higher, reflecting the relatively coarse features associated for the surface. The small-scale smoothness of surface D is reflected in the lower variation at the finer length scales. For the random surface E, the bulk of the variance is explained at the finest level, i.e., the level of noise.

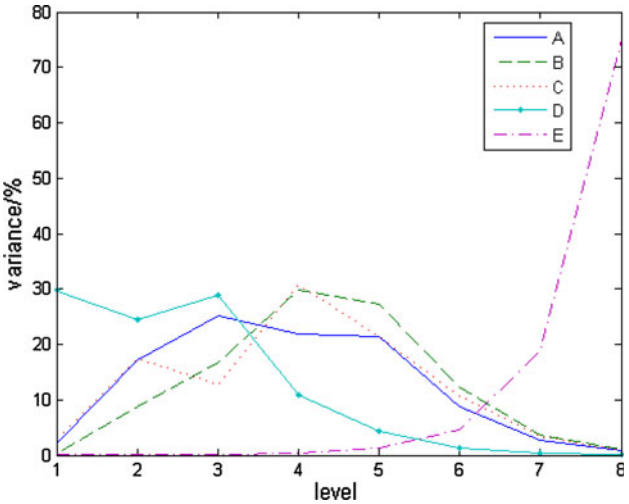

Fig. 9 Partition of variances, as a percentage of the total variation, of surfaces A, B, C, D and E, at levels 1 to 8, coarse to fine, based on a Haar wavelet decomposition. The values for the different levels are joined by straight-line segments for purposes of visualisation

A measure of the difference between variance profiles is given by the χ^2 test [28] for comparing frequency distributions. Regarding the computed variances at each level,

Table 2 Values of χ^2 calculated in (2) for five surfaces A, B, C, D and E, derived from a partition of variances present in Fig. 9

	B	C	D	E
A	8.68	5.92	48.58	169.24
B		6.51	77.94	163.69
C			61.08	165.50
D				188.82

represented in Fig. 9, as observed sample rates, $f_{A,k}$, $f_{B,k}$, etc., from a distribution with 8 states (the levels or scales), then the χ^2 values are defined by

$$\chi^2_{A,B} = \sum_{k=1}^{8} \frac{(f_{A,k} - f_{B,k})^2}{f_{A,k} + f_{B,k}}, \tag{2}$$

etc., and give a measure of how likely it is that two profiles are drawn from the same probability distribution. The observed χ^2 values can be compared with the quantiles of the χ^2 distribution χ^2_ν with $\nu = 8 - 1$ degrees of freedom. The expected value of a draw from χ^2_7 is 7 and there is a 5 % probability that it exceeds a value of 14.1. Table 2 gives the χ^2 values calculated as in (2) for each pair of surfaces. On this basis, surfaces A, B, and C are differentiated from surface D and all are differentiated from surface E, but that there is no significant difference between surfaces A, B and C at the 95% level.

3.2.2 *Within- and between-group measures*

The Haar wavelet decomposition of the surface uses a partition of the grid at various levels, from coarse to fine. An alternative approach is to use the same type of nested partition of the surface and compare surface parameters evaluated on each subgrid. For example, let $n_{k,pq}$ be the number of grid points in the pqth subgrid at level k, and $\bar{z}_{k,pq}$ and $s^2{}_{k,pq}$ the corresponding mean height and variance. The total variation Sq^2 for the surface can be written as $Sq^2 = B_k + W_k$ where B_k and W_k represent the between- and within-group variances:

$$B_k = \sum_{p,q} n_{k,pk}(\bar{z}_{k,pq} - \bar{z})^2,$$

$$W_k = \frac{1}{N_x N_y - 1} \sum_{p,q} (n_{k,pq} - 1) s^2_{k,pq}.$$

Here, $\bar{z}$ is the mean surface height for the complete surface. For a surface with the least-squares best-fit plane removed, $\bar{z} = 0$. For a flat, homogeneous surface, we expect B_k to be small relative to Sq^2. Conversely, if B_k is large relative to Sq^2, there is evidence of inhomogeneity at the kth level.

If the grid size is given by powers of two, e.g., 128 × 128 or 256 × 256, the Haar wavelet decomposition coincides with the within- and between-group analysis with the ratios R_k defined in (1) given by

$$R_k = B_k/(B_k + W_k) = B_k/Sq^2.$$

In this sense, the wavelet decomposition captures the balance between fine and coarse scale variation.

Using a partition into subgrids, any measure of surface behaviour can be calculated for each subgrid, and the variation in measures over the complete surface quantified. For example, let $Sq_{k,pq}$ be the surface roughness parameter Sq calculated for the pqth subgrid in the kth level partition. Each value of $Sq_{k,pq}$ is calculated after the least-squares best-fit plane has been removed from the heights z_{ij} for the pqth subgrid. By contrast, in the wavelet analysis the least-squares best-fit plane is removed only from the complete surface.

We have computed $Sq_{k,pq}$ for the five surfaces A, B, C, D and E for the case $k = 5$ so that each surface is divided into $32 \times 32 = 1024$ subgrids. Since we are interested in the variation of the Sq values over the surface, we set

$$s_{pq} = Sq_{5,pq}/\bar{Sq}_5, \tag{3}$$

where $\bar{Sq}_5$ is the average over p and q of $Sq_{5,pq}$. Thus, for each surface s_{pq} is scaled so that their average is equal to one. The s_{pq} are then sorted into bins $j = 1,\ldots,n_B$, with the bins widths chosen so that, averaged over the four surfaces A, B, C and D, the numbers in the bins are approximately equal. The bin counts $f_{A,j}$, etc., for the five surfaces can then be compared using a χ^2 measure as in (2) but with the index k replaced by j.

Figure 10 graphs the distribution of s_{pq} for the four surfaces A, B, C and D and eight bins while Table 3 gives the χ^2 values which can be compared with 95% quantile value of 14.1 of the corresponding χ^2_7 distribution. Figure 10 shows that for surfaces A and C most subgrids have Sq values close to the average value, surface B has Sq values distributed approximately equally over the range while surface D has relatively few subgrids with an Sq value near the average value. Table 3 shows that only surfaces A and C are comparable with each other.

The χ^2 values give a measure of the difference between distributions, but what can be said about the homogeneity of the surfaces? Table 4 shows the standard deviations of the s_{pq} values for the five surfaces and shows that, by this measure, surface A (0.43) and C (0.44) have similar variation, B (0.51) slightly more and D (0.73) more again. The random surface E (0.05) is the most homogeneous, as can be expected.

An alternative measure of variation is given by the relative (information) entropy, also known as the Kullback–Leibler divergence [29, 30], a method of comparing one distribution with another. Given two discrete distributions p_j and q_j with $\sum_j p_j = \sum_j q_j = 1$, the relative entropy is defined by

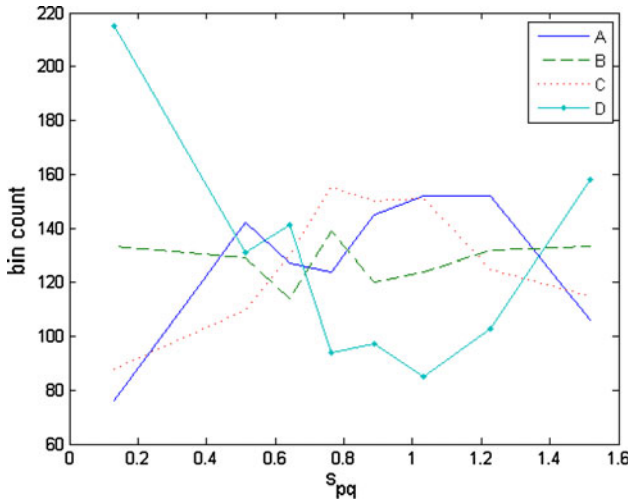

Fig. 10 Bin counts of s_{pq}, normalised values of Sq for surfaces A, B, C and D calculated over 32 × 32 subgrids

Table 3 Values of χ^2 calculated in (2) for bin counts of s_{pq}, defined in (3), over a 32 × 32 partition for the five surfaces A, B, C, D and E

	B	C	D	E
A	27.38	11.51	119.82	546.69
B		20.07	46.33	627.46
C			109.18	568.70
D				669.49

Table 4 Values for standard deviation, s, and relative entropy, D_{KL}, derived from bin counts of s_{pq} values, (3), over a 32 × 32 partition for the five surfaces A, B, C, D and E

	A	B	C	D	E
s	0.43	0.51	0.44	0.73	0.05
D_{KL}	0.0289	0.003	0.0218	0.0681	2.1322

$$D_{\mathrm{KL}}(p|q) = \sum_j p_j \log_2(p_j/q_j).$$

Relative entropy has the property that $D_{\mathrm{KL}}(p|q) \geq 0$ with equality only if $p_j = q_j$, for all j. However $D_{\mathrm{KL}}(p|q)$ is not generally equal to $D_{\mathrm{KL}}(q|p)$. If the distributions p and q represent the state-of-knowledge about a parameter then $D_{\mathrm{KL}}(p|q)$ is a measure of the information gain of p over q.

If the observed s_{pq} are binned in a histogram and f_j is the relative frequency associated with the jth bin so that $\sum_j f_j = 1$, then the entropy of f_j relative to another distribution p_j can be calculated. Relative entropy may be more appropriate than the standard deviation as a measure of dispersion for structured surfaces in which two or more types of behaviour are prevalent. Table 4 also gives $D_{\mathrm{KL}}(f_j|q_j = 1/8)$ comparing f_j with a uniform distribution across the 8 bins, so that the D_{KL} value represents some measure of structure in the surface relative to the average structure of the four surfaces. The table shows that surface D is more 'structured' than A, B or C. The ordering of the D_{KL} values is not the reverse of that for the standard deviation values.

3.3 Local analysis using linear filters

The wavelet analysis is an example of (global) regression analysis. The properties of the surface are characterised in terms of how well the surface heights can be matched by a particular type of model surface. For example, for the Haar wavelet, the model surface is a step function, constant over each subgrid. For linear regression models, the approximation function can usually be written as

$$\phi(x, y, \mathbf{a}) = \sum_{k=1}^{n} a_k \phi_k(x, y),$$

where $\phi_k(x, y)$ are basis functions. Given data points $\mathbf{x}_{ij} = (x_{ij}, y_{ij}, z_{ij})^{\mathrm{T}}$, $i = 1,...,N_x$, $j = 1,...,N_y$ the estimate $\mathbf{a} = (a_1, \ldots, a_n)^{\mathrm{T}}$ of the coefficients that minimise the sum of squares

$$\sum_{i=1}^{N_x} \sum_{j=1}^{N_y} (z_{ij} - \phi(x_{ij}, y_{ij}, \mathbf{a}))^2,$$

is given by

$$\mathbf{a} = C^{\dagger}\mathbf{z}, \quad C^{\dagger} = \left(C^{\mathrm{T}}C\right)^{-1}C^{\mathrm{T}}, \quad C = [\mathbf{c}_1 \cdots \mathbf{c}_n],$$

where $\mathbf{c}_k$ and $\mathbf{z}$ are the vectors of length $m = N_x N_y$ storing $\phi_k(x_{ij}, y_{ij})$, $k = 1,...,n$, and z_{ij}, respectively. An important feature of linear regression analysis is that the solution parameters $\mathbf{a}$ are given as a linear combination defined by the $n \times m$ matrix $C^{\dagger}$ of the data vector $\mathbf{z}$.

In regression analysis, the parameter estimates $\mathbf{a}$ represent features of the complete surface extracted from the data vector $\mathbf{z}$. The main idea of a filter is to extract, for each point $(x_{pq}, y_{pq})^{\mathrm{T}}$ on the grid, a feature or features $\mathbf{a}_{pq}$ using only those heights z_{ij} corresponding to grid points $(x_{ij}, y_{ij})^{\mathrm{T}}$ local to $(x_{pq}, y_{pq})^{\mathrm{T}}$. For example, regarding the pqth point as being at the centre of a 3 × 3 grid, a_{pq} could be taken as the average height of the nine points in the local grid. Linear filters can be described more generally as follows. Let Z be the $N_x \times N_y$ matrix of heights with $Z(i, j) = z_{ij}$ and let F be any $n \times n$ matrix where n is odd and much smaller than N_x and N_y. For indices $(n + 1)/2 \leq p \leq N_x - (n - 1)/2$, and $(n + 1)/2 \leq q \leq N_y - (n - 1)/2$, set Z_{pq} to be the $n \times n$ submatrix of Z centred at location (p, q) and define

$$Z_F(p, q) = \sum_{i=1}^{n} \sum_{j=1}^{n} F(i,j) Z_{pq}(i,j)$$

to be the output of the filter defined by F at location (p, q). The quantity $Z_F(p, q)$ is a measure of how much Z is correlated with F at location (p, q). Importantly, the output Z_F can be calculated very efficiently using the 2-dimensional fast Fourier transform [31, 32].

Different choices of filter F will highlight different aspects of the behaviour of the surface. Let W be an $n \times n$ weighting matrix with $W(i, j) = w_{ij}$, n odd, and Φ_k a set of $n \times n$ matrices or masks representing basis functions evaluated on an $n \times n$ grid of x- and y-co-ordinates. For submatrix Z_{pq}, the weighted least-squares best-fit combination of masks Φ_k to Z_{pq} is given by the **a** that minimises

$$\sum_{i,j=1}^{n} w_{ij}^2 (Z_{pq}(i,j) - \Phi_{\mathbf{a}}(i,j))^2, \quad \Phi_{\mathbf{a}}(i,j) = \sum_k a_k \Phi_k(i,j). \tag{4}$$

As mentioned above, a property of the solution of a linear least-squares fitting problem is that each solution parameter is a linear combination of the data being fitted. For (4), this means that each solution a_k can be evaluated using a mask $A_k = \{A_k(i, j)\}$ defined in terms of Φ_k:

$$a_k(p,q) = \sum_{i,j=1}^{n} A_k(i,j) Z_{pq}(i,j).$$

Furthermore, the value of the fitted function and residual at location (p, q) can also be evaluated using appropriate filters derived from Φ_k.

For example, suppose we wish to find the best fit plane $\phi = a_1 + a_2 x + a_3 y$ to z_{ij} for each 3×3 submatrix Z_{pq} of Z. It is straightforward to show that the parameters a_k, $k = 1, 2, 3$, can be determined using 3×3 filters:

$$A_1 = \frac{1}{9}\begin{bmatrix} 1 & 1 & 1 \\ 1 & 1 & 1 \\ 1 & 1 & 1 \end{bmatrix}, \quad A_2 = \frac{1}{18}\begin{bmatrix} -3 & -3 & -3 \\ 0 & 0 & 0 \\ 3 & 3 & 3 \end{bmatrix},$$
$$A_3 = \frac{1}{18}\begin{bmatrix} -3 & 0 & 3 \\ -3 & 0 & 3 \\ -3 & 0 & 3 \end{bmatrix}, \tag{5}$$

the height of the best-fit plane at the central location is also calculated using the filter A_1 and that the residual at the central location is calculated using the filter

$$\frac{1}{9}\begin{bmatrix} -1 & -1 & -1 \\ -1 & 8 & -1 \\ -1 & -1 & -1 \end{bmatrix}.$$

Using the filters A_1, A_2 and A_3, the parameters of the best fit plane

$$z = a_{1,pq} + a_{2,pq} x + a_{3,pq} y, \tag{6}$$

for nine heights centred at each (x_p, y_q) can be calculated, from which the slope magnitude and angle of inclination

$$m_{pq} = \frac{\left(\left(\frac{a_{2,pq}}{\Delta x}\right)^2 + \left(\frac{a_{3,pq}}{\Delta y}\right)^2\right)^{1/2}}{\left(1 + \left(\frac{a_{2,pq}}{\Delta x}\right)^2 + \left(\frac{a_{3,pq}}{\Delta y}\right)^2\right)^{1/2}}, \quad A_{pq} = \tan^{-1} m_{pq}, \tag{7}$$

respectively, can be derived; here Δx and Δy are the grid spacing in the x and y directions. From the set of calculated slopes and angles, their mean, standard deviation, skewness, etc. can be calculated.

3.4 Local analysis using nonlinear filters

The significant advantage of linear filters is that they can be computed using extremely efficient convolution algorithms. However, the same approach of moving a finite window over the surface and calculating parameters that are a nonlinear function of the heights that fall inside the window can also be applied. Below we discuss a few examples.

3.4.1 Density of summits (Sds)

The density of summits parameters *Sds* is the number of summits in a unit sampling area. The height z_{pq} is regarded as a summit if it is higher than its eight nearest neighbours and can be determined using a 3×3 window. The associated nonlinear filter returns 1 if z_{pq} is a summit, 0 otherwise.

For a surface represented by an $N_x \times N_y$ matrix of heights corresponding to a regular grid of x- and y-co-ordinates with spacing Δx and Δy, then

$$Sds = \frac{n_S}{(N_x - 1)(N_y - 1)\Delta x \Delta y},$$

where n_S is the number of summits.

Table 1 gives the calculated *Sds* parameter for the five surfaces A, B, C, D and E. The locally smooth character of surface D is reflected in the relatively small *Sds* value. Similarly, the random nature of surface E leads to a very high *Sds* value.

3.4.2 Local (weighted) roughness parameter (Sq_{pq})

Given an $n \times n$ weight matrix W with $w_{ij} \geq 0$, and n odd, then the local *Sq* value at position (p, q), can be calculated as follows. First a plane is fitted to the heights in the $n \times n$ matrix Z_{pq} of heights centered at (p, q) and Z_{pq} is overwritten with the adjusted heights. Secondly, the local roughness parameter at (p, q), $Sq(p, q)$, is calculated according to

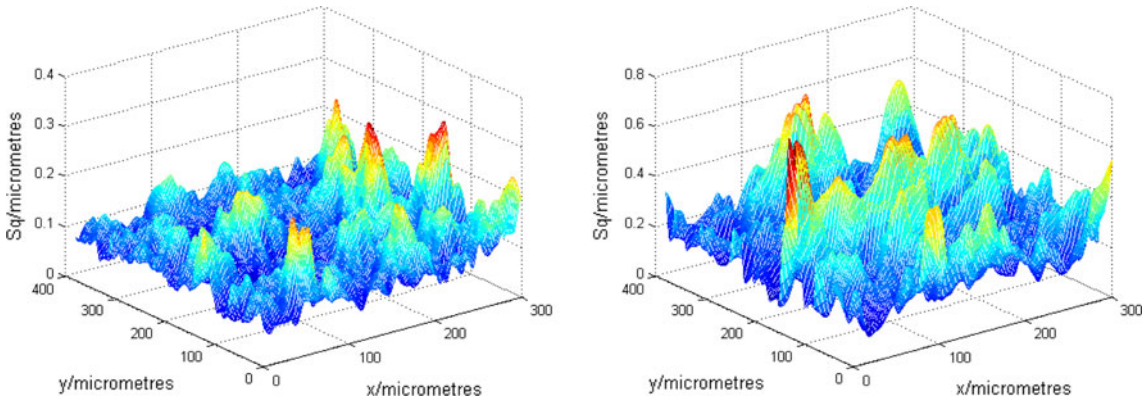

Fig. 11 Surface roughness $Sq(p, q)$ for surfaces A (*left*) and B (*right*), calculated over a 25 μm × 25 μm window, i.e., a 31 × 31 subgrid

$$Sq(p,q) = \frac{1}{n}\left[\sum_{i,j=1}^{n} w_{ij}^2 Z_{pq}(i,j)^2\right]^{1/2}.$$

If the weight matrix is normalised so that $\sum_{i,j=1}^{n} w_{ij}^2 = n^2$, then the expected value of $Sq(p, q)$ for a purely random surface $z_{ij} \in \mathrm{N}(0, \sigma^2)$ will be σ.

Figures 11 and 12 gives the local surface roughness maps for surfaces A, B, C and D calculated over a 31 × 31 pixel grid corresponding to a 25 μm × 25 μm subgrid using unit weights. Figure 13 gives the histograms of $Sq(p, q)/Sq$ for the four surfaces. For each of the four surfaces, the average of the ratio $Sq(p, q)/Sq$ is significantly smaller than 1, indicating that the local roughness is smaller than the global roughness. For surface D, the reduction is most marked, giving another indication of its smoothness at smaller scales.

3.5 Spatial isotropy

The surface features considered so far do not reflect to any great extent the way the behaviour of the surface changes with respect to direction along the surface. We now discuss a number of features that are designed to examine how the surface changes with direction.

3.5.1 *Directions of greatest slope*

By definition, a slope represents a change in height in a given direction. The parameters of the best-fit plane in (6) calculated using the linear filters defined in (5) determine the direction vector $\mathbf{n}_{pq}$ and angle θ_{pq}

$$\mathbf{n}_{pq} = (a_{2,pq}/\Delta x, a_{3,pq}/\Delta y)^{\mathrm{T}}/m_{pq}, \quad a_{2,pq} = (\Delta x) m_{pq} \cos\theta_{pq},$$
$$a_{3,pq} = (\Delta y) m_{pq} \sin\theta_{pq},$$

respectively, (with m_{pq} calculated as in (7)) of steepest slope at location (p, q). The angles θ_{pq} can be binned in a histogram to give the frequency f_j at which angles in the interval $[\theta_j, \theta_{j+1}]$ appear as the directions of steepest slope. The ratio

$$Sl = \min_j f_j / \max_j f_j, \quad 0 \le Sl \le 1, \tag{8}$$

is a measure of lay, i.e., surface directionality: the smaller the value of Sl, the higher the anisotropy. This parameter can be computed efficiently as it is derived from an

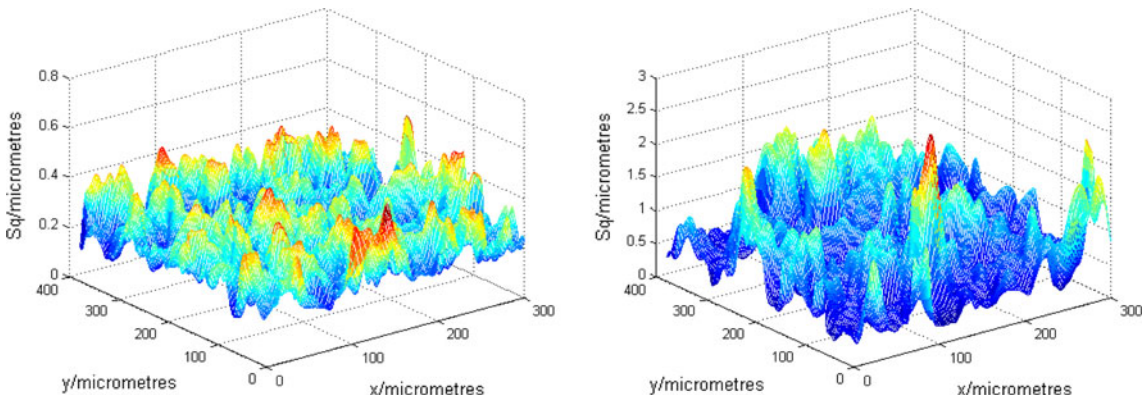

Fig. 12 As Fig. 11 but for surfaces C (*left*) and D (*right*)

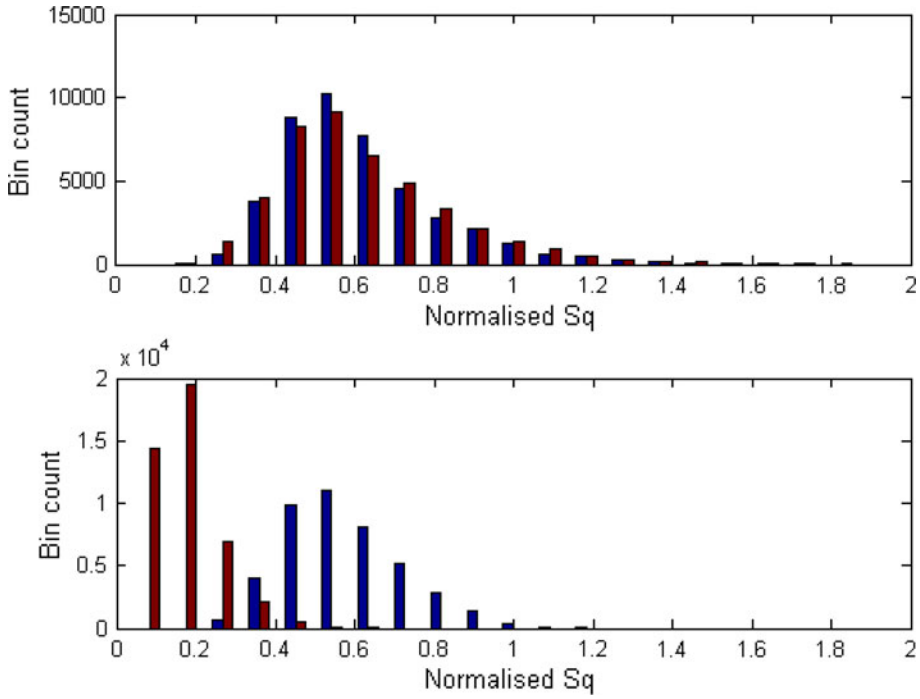

Fig. 13 Histograms of $Sq(p, q)/Sq$ for surfaces A (top, righthand bars), B (top, lefthand bars), C (bottom, righthand bars) and D (bottom, lefthand bars)

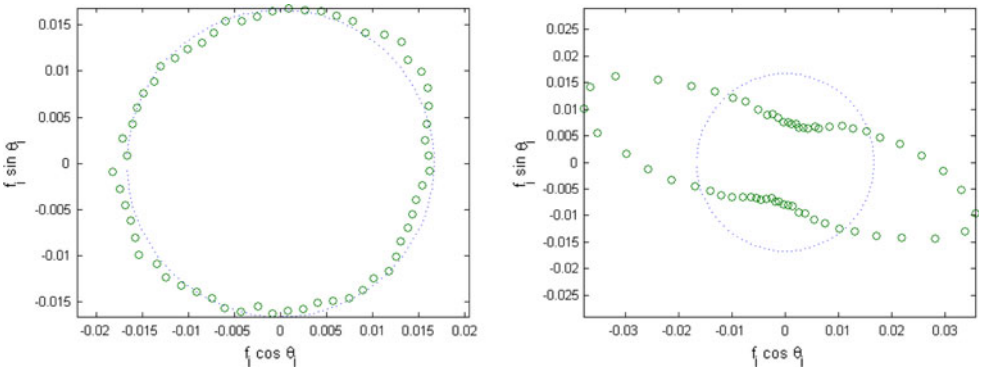

Fig. 14 Normalized bin counts f_j for direction of maximum slope as a function of angle for ground surfaces A (*left*) and B (*right*). The dotted circle gives the expected normalised bin count for a completely isotropic surface

application of a simple linear filter. Table 1 gives the calculated *Sl* parameter for the five surfaces A, B, C, D and E. The grooved topography of surface B (see Figs. 3, 5) is very apparent in the correspondingly low value of *Sl*. A graphical representation of the directionality of slope can be given by plotting the relative bin count f_j against angle θ_j in polar co-ordinates; see Figs. 14 and 15. Table 5 gives the standard deviation and relative entropy associated with the relative frequencies if the direction angles θ_{pq} are assigned to eight bins. The directional nature of surface B is clearly reflected in the calculated values.

3.5.2 Autocovariance function

For a surface represented by an $N_x \times N_y$ matrix Z of heights corresponding to a regular grid of x- and y-co-ordinates, the autocovariance function can be considered as the result of applying a linear filter F to Z, Sect. 3.3, where the filter F is the equal to surface Z itself. The filtered surface Z_F will be represented by a $(2N_x - 1) \times (2N_y - 1)$ matrix, scaled so that the central value is 1. The autocovariance at location (p, q) measures the similarity of the surface with the itself translated by p in x and q in y. The autocovariance values will decay from the maximal central value as the distance measure $(p^2 + q^2)$ increases, with the rate of decay depending on the autocorrelation along the direction specified by (p, q). The parameter *Str*, known as the surface texture aspect ratio [25], is a measure of the fastest decay relative to the slowest decay and is given in terms of the ratio of the shortest distance from the centre at which the autocovariance has decayed to 0.20 (or some other specified value) to the largest such distance. Although the autocovariance function can be calculated using convolution techniques, the fact that the filter is large in dimension means that the autocovariance function can be computationally expensive to calculate.

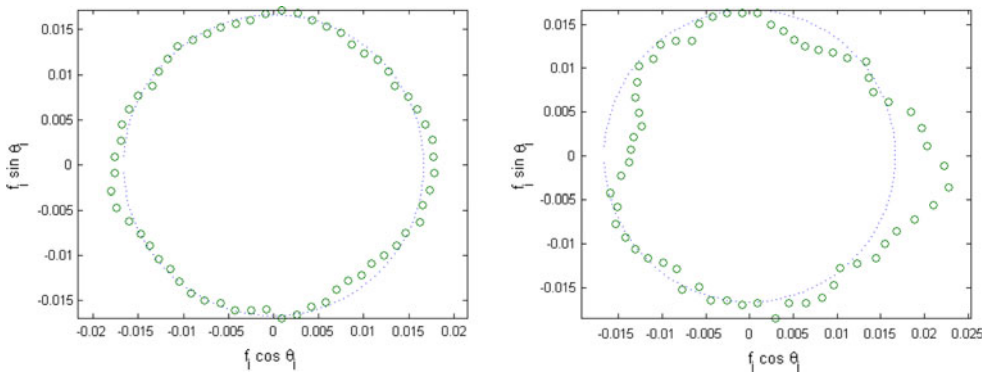

Fig. 15 As Fig. 14 but for surfaces C (*left*) and D (*right*)

Table 5 Standard deviation (s) and relative entropy (D_{KL}) values derived from bin counts for maximal slope direction angles for five surfaces A, B, C, D and E

	A	B	C	D	E
s	0.0051	0.0712	0.0029	0.0140	0.0010
D_{KL}	0.0010	0.1914	0.0003	0.00077	0.0000

Table 1 gives the *Str* parameter values for the five surfaces A, B, C, D and E. The grooved nature of surface B is reflected in the small value of *Str*. Figures 16 and 17 shows the autocovariance functions for surfaces B and C. The autocovariance for surface B is seen to be largest in the direction of the grooves (Fig. 5).

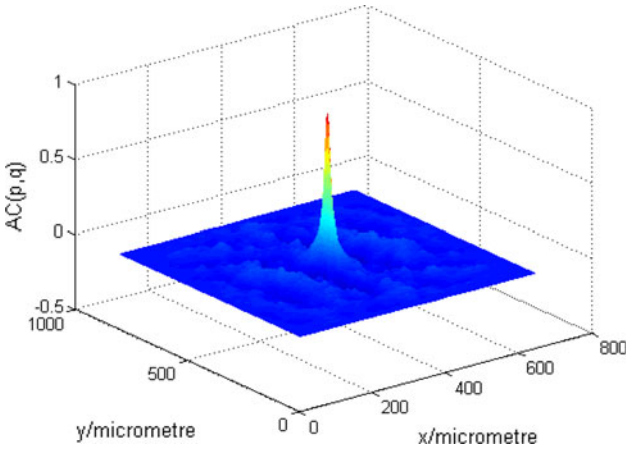

Fig. 17 Autocovariance function for surface C

4 Correlating cell behaviour and surface topography

4.1 Analysis of binary image data

The cell imaging techniques discussed in Sect. 2.3 enable a digital representation of cell occupation. Figures 18 and 19 show three cell masks represented as binary matrices, M1, M2 and M3, where a one indicates that a cell is present and a zero (graphed as white) indicates no cell. The masks were determined from cell images on three ground surfaces; for example, mask M3 is associated with the surface shown in Figs. 1 and 2. (Masks M1 and M2 are associated with ground surfaces similar to that associated with M3 but not graphed in this paper. Surfaces A, B, C and D have been used in this paper only to illustrate the behaviour of the surface analysis algorithms). The binary image data can be analysed using a number of techniques to determine the extent cell shape and density correlate with surface texture and lay.

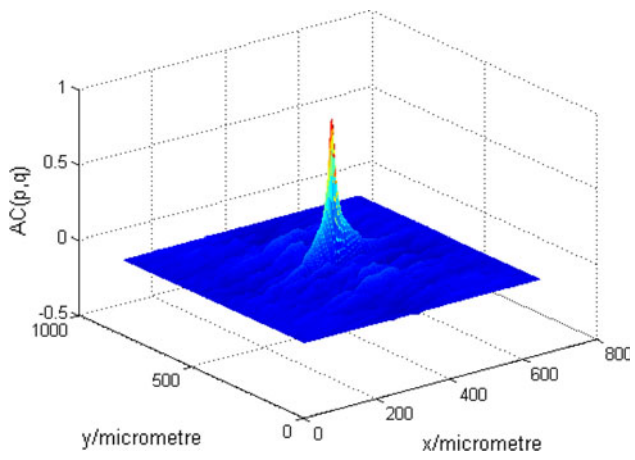

Fig. 16 Autocovariance function for surface B

4.1.1 Density of cells

The simplest feature to compute is a measure of the density of cells ρ_C given by the number n_C of grid points with mask value 1 divided by the total number $N_x \times N_y$ of grid points

$$\rho_C = \frac{n_C}{N_x N_y}.$$

4.1.2 Extent of boundary calculations

Using a linear filter it is possible to identify those grid points that are on the boundary of a cell, as represented by

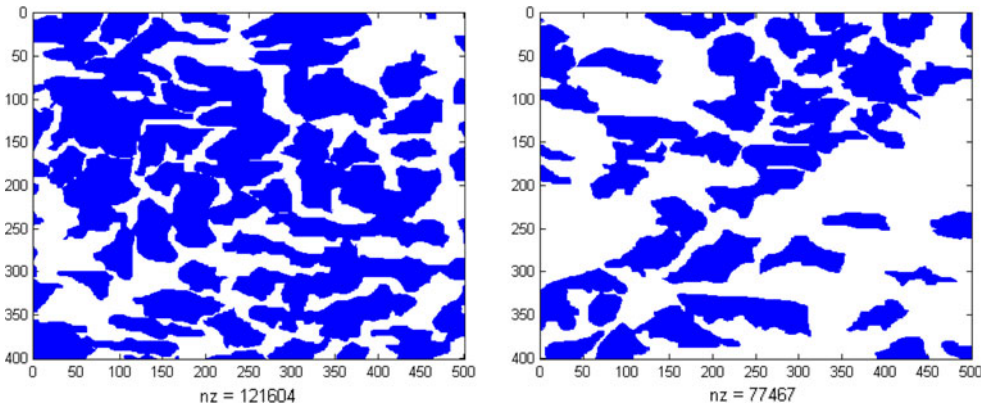

Fig. 18 Binary matrices M1 and M2, left and right, respectively, representing cell masks on two ground surfaces; white regions denote absence of cells (The figures are produced by the Matlab 'spy' function which gives the count *nz* of the nonzero elements)

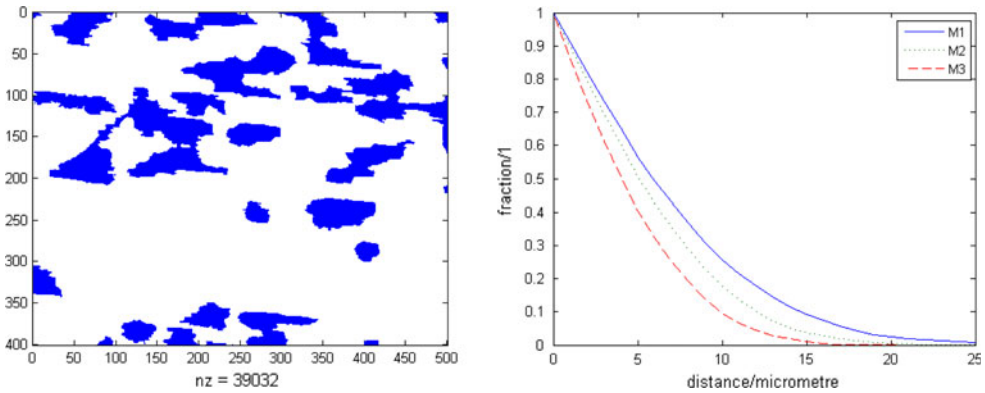

Fig. 19 *Left*: binary matrix representing the cell mask M3 for the ground surface shown in Fig. 1. *Right*: the fraction of cell grid points at least distance D from a boundary point for masks M1 (solid), M2 (dotted) (Fig. 18) and M3 (dashed)

the mask. The ratio of the number of boundary points to interior points gives an average measure of how elongated or irregular the cell shapes are.

4.1.3 Cell radii

In a similar calculation to that for the boundary calculations, for a given threshold distance D, it is possible to use linear filters to identify the number $n(D)$ of grid points that are in the interior of a cell and at least distance D from a boundary point. By varying D and calculating $n(D)$ it is possible to derive further characteristics of the cell shapes.

In Figs. 18 and 19, the densities of cells for the three masks are 61%, 39% and 20%, and the ratios of boundary to interior are 8.1%, 9.5% and 13.0%, respectively. Figure 19 also gives the fraction of cell grid points $f(D) = n(D)/n_C$ at least distance D from a boundary for the three masks. It is seen that the increasing elongation of cell clusters from M1 to M3 is reflected in the increase in boundary-to-interior ratios and the reduction in $f(D)$.

4.1.4 Mask autocovariance

The autocovariance function can also be calculated for a mask. Figure 20 shows the autocovariance corresponding to mask M3 in Fig. 19. The autocovariance function gives quantitative evidence that the cells are aligned with the grooved topography of the underlying surface, Figs. 1, 2, a behaviour discernible in the mask itself.

5 Summary and concluding remarks

This paper has been concerned with defining and comparing quantitative methods for analysing surface topography and

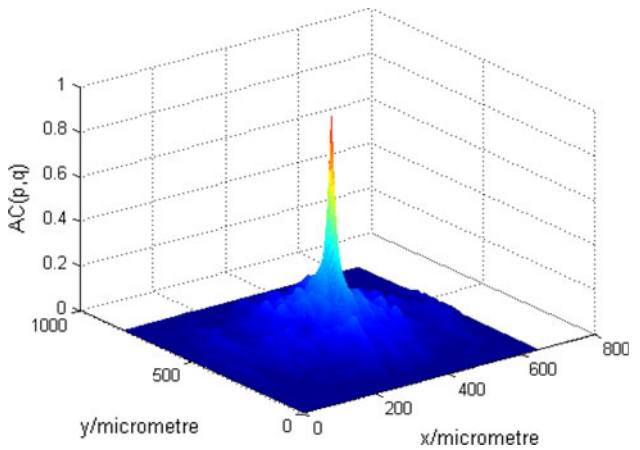

Fig. 20 The autocovariance function associated with mask M3 (Fig. 19, *left*)

Table 6 Summary of advantages and disadvantages of the analysis methods

Analysis method	Advantages	Disadvantages
Global surface analysis	Universal application; gives easy to understand summary information, often with a statistical interpretation; creates a baseline for comparison with local results; easy to compute	Can be overly sensitive to outlying data due to scratches, dust particles;provides no information about variation at a local level; ignores spatial and orientation content
Haar wavelet analysis	Provides frequency content at any given location; decomposes the total surface variation in terms of variation at various length scales; the partition of the total the energy across the different length scales can be used to compare surfaces; can be computed efficiently using the fast Fourier transform	Less sensitive to directional features not aligned with the axes system associated with the wavelets
Analysis on partitions	Provides a similar analysis as a wavelet analysis, and allows an assessment of inhomogeneity to be made	Poor sensitivity to directional features not aligned with the data axes
Linear filter analysis	Extremely flexible; able to isolate specific features through appropriate filter design, e.g., directional features; canbe implemented efficiently used the fast Fourier transform	Effectiveness depends of the choice of appropriate filter
Nonlinear filter analysis	As for linear filter	As for linear filter; cannot be computed by the fast Fourier transform
Autocovariance	Comprehensive method identifying patterned or directional behaviour	Although a type of linear filter analysis, it is computationally expensive for large data sets

cell adhesion on the basis of features derived from 3D-microscopy data. The surface topography features discussed include standard parameters used to describe surface roughness behaviour but also features that capture topographical surface texture at various length scales, using wavelet analysis, for example, or the degree of heterogeneity and anisotropy using a local analysis based on linear and nonlinear filters.

For data representing a set of heights at a regular grid of points, the main idea of a local analysis is straightforward. Any parameter that can be calculated globally for all the data can be calculated for a finite window centred at a grid point. The value of the parameter at a grid point now defines a new set of heights that can be the subject of further analysis. In particular, the variation of the parameter values, as estimated by a standard deviation, range or relative entropy, gives a measure of the heterogeneity. Similarly, any parameter that specifies a direction can be used in a local analysis to examine the behaviour of the surface in a particular direction. At a minimum, a local analysis replaces one parameter with two, e.g., replacing a global value of the roughness parameter *Sq* with the mean *Sq* value and standard deviation of *Sq* as it varies over the surface. Table 6 gives a summary of the analysis methods discussed in this paper.

While the extraction of functionally relevant features from surface data is difficult, the analysis of cell behaviour is usually more difficult since large randomising effects are likely to be present. A major step is to be able to codify the presence of cells in a digital mask. If this can be achieved reliably, then the computational tools can be applied to the mask in order to derive informative features. We have shown that by using linear filter techniques or similar, it is possible to extract information on cell density, size, shape and orientation.

Given a set of observed topography features and measures of cell size, shape and orientation for a range of surface textures, a final stage of analysis can be attempted a) to determine which topographical features are most important in explaining the observed cell behaviour, and b) to predict cell behaviour for a particular surface on the basis of known surface texture features. In this final stage, techniques such as principle component analysis, partial least squares, etc., will likely be important. However, in order to extract significant relationships in the presence of large random effects it will likely be necessary to have an more extensive set of experimental data than that acquired in the current study.

Acknowledgements The authors gratefully acknowledge the support of the UK's Department of Innovation, Universities and Skills Measurement for Emerging Technologies and Software Support for Metrology Programmes.

References

1. Flemming RG, Murphy CJ, Abrams GA, Goodman SL, Nealey PF. Effects of synthetic micro- and nano-structured surfaces on cell behavior. Biomaterials. 1999;20:573–88.
2. Wirth C, Grosgogeat B, Lagneau C, Jaffrezic-Renault N, Ponsonnet L. Biomaterial surface properties modulate in vitro rat calvaria osteoblasts response: Roughness and or chemistry? Mat Sci Eng C. 2008;28:990–1001
3. Zhao G, Schwartz Z, Wieland M, Rupp F, Geis-Gerstorfer J, Cochran DL, Boyan BD. High surface energy enhances cell response to titanium substrate microstructure. J Biomed Mater Res A. 2005;74:49–58

4. Clark P, Connolly P, Curtis ASG, Dow JAT, Wilkinson CDW. Topographical control of cell behaviour. 1. Simple step cues. Development. 1987;99:439–48
5. Britland S, Perridge C, Denyer M, Morgan H, Curtis ASG, Wilkinson CDW. Morphogenetic guidance cues can interact synergistically hierarchically in steering nerve cell growth. Exp Biol Online 1996;1:2.
6. Charest JL, Eliason MT, Garcia AJ, King WP. Combined microscale mechanical topography and chemical patterns on polymer cell culture substrates. Biomaterials. 2006;27:2487–94.
7. den Braber ET, Deruijter JE, Smith HTJ, Ginsel LA, Vonrecum AF, Jansen JA. Effect of parallel surface microgrooves and surface energy on cell growth. J Biomed Mater Res. 1995;29:511–8.
8. Wieland M, Chehroudi B, Textor M, Brunette DM. Use of Ti-coated replicas to investigate the effects on fibroblast shape of surfaces with varying roughness and constant chemical composition. J Biomed Mater Res. 2002;60:434–44.
9. Zhao G, Raines AL, Wieland M, Schwartz Z, Boyan BD. Requirement for both micron- and submicron scale structure for synergistic responses of osteoblasts to substrate surface energy and topography. Biomaterials. 2007;28:2821–9.
10. Clark P, Connolly P, Curtis ASG, Dow JAT, Wilkinson CDW. Topographical control of cell behaviour.2. Multiple grooved substrata. Development. 1990;108:635–44.
11. Andersson A-S, Brink J, Lidberg U, Sutherland DS. Influence of systematically varied nanoscale topography on the morphology of epithelial cells. IEEE Trans Nano Biosci. 2003;2:49–57.
12. Lim JY, Donahue HJ. Cell sensing and response to micro- and nanostructured surfaces produced by chemical and topographic patterning. Tissue Eng. 2007;13:1879–91.
13. Variola F, Yi JH, Richert L, Wuest JD, Rosei F, Nanci A. Tailoring the surface properties of Ti6Al4V by controlled chemical oxidation. Biomaterials. 2008;29:1285–98.
14. Dalby MJ, Gadegaard N, Tare R, Andar A, Riehle MO, Herzyk P, Wilkinson CDW, Oreffo ROC. The control of human mesenchymal cell differentiation using nanoscale symmetry and disorder. Nature Mat. 2007;6:997–1003.
15. Ranucci CS, Moghe PV. Substrate microtopography can enhance cell adhesive and migratory responsiveness to matrix ligand density. J Biomed Mater Res A. 2001;54:149–61.
16. Curtis ASG, Clark P. The effects of topographic and mechanical properties of materials on cell behavior. Crit Rev Biocompat. 1990;5:343–62.
17. Curtis ASG, Wilkinson C. Topographical control of cells. Biomaterials. 1997;18:1573–83.
18. Curtis ASG. Small is beautiful but smaller is the aim: review of a life of research. Eur Cell Mater. 2004;8:27–36.
19. ISO 4287 2000 Geometrical Product Specifications (GPS). Surface Texture: Profile Method—Terms, Definitions and Surface Texture Parameters (International Organization for Standardization).
20. Tete S, Mastrangelo F, Traini T, Vinci R, Sammartino G, Marenzi G, Gherlone E. A macro- and nanostructure evaluation of a novel dental implant. Implant Dent. 2008;17:309–16.
21. Le Guehennec L, Lopez-Heredia M-A, Enkel B, Weiss P, Amouriq Y, Layrolle P. Osteoblastic cell behaviour on different titanium implant surfaces. Acta Biomater. 2008;4:535–43.
22. Dong WP, Sullivan PJ, Stout KJ. Comprehensive study of parameters for characterizing 3-dimensional surface topography.3. Parameters for characterizing amplitude and some functional properties. Wear. 1994;178:29–43.
23. Dong WP, Sullivan PJ, Stout KJ. Comprehensive study of parameters for characterizing 3-dimensional surface topography.4. Parameters for characterizing spatial and hybrid properties. Wear.1994;178:45–60.
24. Sosale G, Hacking SA, Vengallatore S. Topography analysis of grit-blasted and grit-blasted-acid-etched titanium implant surfaces using multi-scale measurements and multi-parameter statistics. J Mater Res. 2008;23:2704–13.
25. Blunt L, Jiang X. Advanced techniques for the assessment of surface topography. London: Kogan Page Science; 2003.
26. Forbes AB, Lam J, Tomlins PE. Capturing local and anisotropic behaviour in surface topography. Wear. 2009;266:527–9.
27. ISO/DIS 25178-2 Geometrical product specifications (GPS). Surface texture: Areal—Part 2: Terms, definitions and surface texture parameters, International Organization for Standardisation, Geneva (2008).
28. Snedecor GW, Cochran WG. Statistical methods. Ames: Iowa State University Press; 1989.
29. Kullback S, Leibler RA. On information and sufficiency. Ann Math Statist. 1951;55:79–86.
30. MacKay DJC. Information theory, inference and learning, algorithms. Cambridge: Cambridge University Press; 2003.
31. Gonzalez RC, Woods RE. Digital image processing, 3rd ed. Upper Saddle Valley: Prentice Hall; 2007.
32. Petrou M, Garcia Sevilla P. Image processing: dealing with texture. Chichester: John Wiley & Sons, Ltd.; 2006.